

# Dynamics and Gravitational Wave Signature of Collapsar Formation

C. D. Ott,<sup>1,\*</sup> C. Reisswig,<sup>1</sup> E. Schnetter,<sup>2,3</sup> E. O'Connor,<sup>1</sup> U. Sperhake,<sup>4,1</sup>  
F. Löffler,<sup>2</sup> P. Diener,<sup>2,3</sup> E. Abdikamalov,<sup>2</sup> I. Hawke,<sup>5</sup> and A. Burrows<sup>6</sup>

<sup>1</sup>TAPIR, Mail Code 350-17, California Institute of Technology, Pasadena, CA, 91125, USA

<sup>2</sup>Center for Computation & Technology, Louisiana State University, Baton Rouge, LA 70803, USA

<sup>3</sup>Department of Physics & Astronomy, Louisiana State University, Baton Rouge, LA 70803, USA

<sup>4</sup>Institut de Ciències de l'Espai (CSIC-IEEC), Facultat de Ciències, Campus UAB, E-08193 Bellaterra, Spain

<sup>5</sup>School of Mathematics, University of Southampton, Southampton, UK

<sup>6</sup>Department of Astrophysical Sciences, Princeton University, 4 Ivy Lane, Princeton, NJ 08544, USA

We perform 3 + 1 general relativistic simulations of rotating core collapse in the context of the collapsar model for long gamma-ray bursts. We employ a realistic progenitor, rotation based on results of stellar evolution calculations, and a simplified equation of state. Our simulations track self-consistently collapse, bounce, the postbounce phase, black hole formation, and the subsequent early hyperaccretion phase. We extract gravitational waves from the spacetime curvature and identify a unique gravitational wave signature associated with the early phase of collapsar formation.

PACS numbers: 04.25.D-, 04.40.Dg, 97.10.Kc, 97.60.Bw, 97.60.Jd, 97.60.Lf, 26.60.Kp

There is strong observational evidence linking long gamma-ray bursts (LGRBs) with the death of massive stars in core collapse (e.g., [1]). It appears likely that LGRBs are made in metal-poor progenitors with degenerate iron cores. These may be ordinary massive stars turned into Wolf-Rayet objects by mass loss or binary interactions [2, 3] or, perhaps, peculiar, fully-mixed stars [4, 5]. Both could result in a type-Ibc core-collapse supernova (CCSN) harboring a LGRB central engine. The nature of the latter and the details of the CCSN-LGRB relationship are uncertain. Viable engine settings all require rapid progenitor rotation and include the protomagnetar model (e.g., [6]) and the collapsar scenario [7, 8]. In the latter, the CCSN fails and a black hole (BH) with an accretion disk forms or a weak explosion occurs leading to fallback and BH/disk formation.

In this Letter, we address, for the first time in 3 + 1 general relativity (GR), the formation of spinning BHs in failing CCSNe in the context of the collapsar scenario of LGRBs. Our full GR method allows us to self-consistently follow core collapse, bounce, postbounce evolution, protoneutron star (PNS) collapse, BH formation, and the subsequent early hyperaccretion phase. For the first time, we extract the gravitational wave (GW) signature of a failing CCSN that evolves into a collapsar and track the properties of the nascent BH with the dynamical horizon formalism [9].

Previous work on BH formation in CCSN/LGRB progenitors was limited to spherical symmetry [10–12] and, due to gauge choices, simulations could not be continued beyond BH formation. Multi-D studies either considered isolated NS collapse (e.g., [13]) or BH formation in very massive polytropes [14, 15]. Recently, Sekiguchi & Shibata [16] carried out the first axisymmetric (2D) GR simulation that continued beyond BH formation in a hot polytrope, but did not extract the GW signal.

*Method.* We employ the Zelmani 3 + 1 GR core col-

lapse simulation package [17] which is based on the Cactus framework and the Carpet adaptive mesh refinement (AMR) driver [18], and uses the open-source Einstein-Toolkit for GR curvature (via [19]) and hydrodynamics evolution (via an updated variant of [13]). We extract GWs directly from the spacetime fields using the fully gauge-invariant Cauchy-Characteristic Extraction method of [17, 20]. The simulations are performed in an octant of the Cartesian 3D cube with periodic boundaries on two of the inner faces of the octant and reflection symmetry about the equatorial plane. This limits 3D structure to even  $\ell$  and  $m$  that are multiples of 4. We use 11 levels of AMR, adding levels during collapse and postbounce evolution when needed. In our baseline resolution (BR), the finest resolution is  $\sim 370$  m and  $\sim 92$  m at bounce and BH formation, respectively. We also perform calculations with 20% higher/lower (HR/LR) resolutions and check stability and consistency by monitoring the ADM constraints. They show 2<sup>nd</sup>-order convergence up to bounce and 1<sup>st</sup>-order afterwards. After BH formation, convergence is reduced near the singularity, but the simulations remain consistent and stable. ADM mass and angular momentum are conserved to  $\lesssim 3\%$  in BR runs. All runs are carried out past BH formation, but only LR runs are continued to tens of ms after BH formation.

We employ a hybrid polytropic- $\Gamma$ -law equation of state (EOS; e.g., [21]). It smoothly matches a polytrope described by  $\Gamma_1 \approx 4/3$  at subnuclear densities with one described by  $\Gamma_2 > \Gamma_1$  at supernuclear densities, allowing to capture the stiffening of the nuclear EOS. A  $\Gamma$ -law component (described by  $\Gamma_{\text{th}}$ ) accounts for thermal pressure contributions due to shock heating. We set  $\Gamma_1 = 1.31$  in the collapse phase and choose a rather soft supernuclear EOS by setting  $\Gamma_2 = 2.4$ . This results in a maximum non-spinning PNS gravitational mass of  $\sim 1.7 M_\odot$ , which provides for rapid BH formation, but is below the empirical NS mass limit [22]. We choose  $\Gamma_{\text{th}} = 4/3$  for the

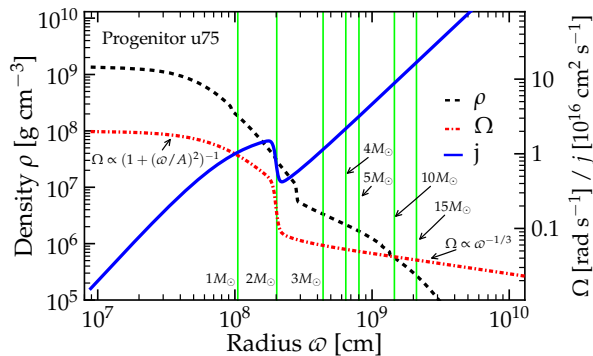


FIG. 1: Progenitor model u75. Left ordinate: Radial density distribution. Right ordinate: Angular velocity (red dash-dotted curve) and specific angular momentum (blue curve) as a function of cylindrical radius  $\varpi$  as given by our rotation law, reproducing features seen in the rotating progenitors of [4]. Vertical lines mark the enclosed mass.

postshock flow whose effective  $\Gamma$  is reduced by the dissociation of Fe-group nuclei. Neutrino heating (unlikely to be dynamically relevant in this scenario) is neglected, but we account for postbounce neutrino cooling of the outer PNS and the postshock region via the cooling function given in [23].

*Initial Conditions.* We use the 75- $M_{\odot}$ ,  $10^{-4}$ -solar metallicity model u75 of [24] whose compact core favors early BH formation [12]. u75 could be a viable GRB progenitor if mass transfer to a binary companion removed its H/He envelopes. We map u75’s inner  $\sim 5700$  km (enclosed mass  $\sim 4.5 M_{\odot}$ ) onto our 3D grid and impose constant rotation on cylindrical shells with radius  $\varpi$  via a rotation law motivated by the GRB progenitors of [4]: The inner iron core is in near uniform rotation and  $\Omega$  drops  $\propto \varpi^{-2}$  further out. Close to the edge of the iron core,  $\Omega$  drops by a factor of order unity, then continues to decrease  $\propto r^{-\zeta}$ , with  $0 < \zeta < 2$ , leading to a radial increase in the specific angular momentum  $j$ , endowing mantle material with sufficient spin to form a disk at small radii. The functional form is  $\Omega(\varpi) = (1 - \lambda(\varpi))\Omega_0(1 + (\varpi/A)^2)^{-1} + \lambda(\varpi)\xi\Omega_0(1 + (\varpi_t/A)^2)^{-1}(1 + (\max(0, \varpi - \varpi_t)/A))^{-\zeta}$ . Here,  $\lambda(\varpi) = (1 + \tanh((\varpi - \varpi_t)/\delta\varpi))/2$ . We set  $A = 1000$  km,  $\varpi_t = 1950$  km,  $\xi = 1/3$ , and  $\delta\varpi = 100$  km.  $\Omega_0$  is the central angular velocity that we vary from 0 to 2  $\text{rad s}^{-1}$ . Fig. 1 depicts u75’s density profile along with  $\Omega(\varpi)$  and  $j(\varpi)$  for the  $\Omega_0 = 2 \text{ rad s}^{-1}$  case. Model names, parameters, and key results are given in Table I.

*Dynamics.*—The homologous collapse of the inner core to nuclear densities proceeds as in the standard CCSN case. For the initial inner core rotation rates considered here, centrifugal effects are negligible in the prebounce phase and all models reach core bounce after  $\sim 114$  ms of collapse. A hydrodynamic bounce shock is launched, but, due to neutrino cooling and the low  $\Gamma$  in the postshock

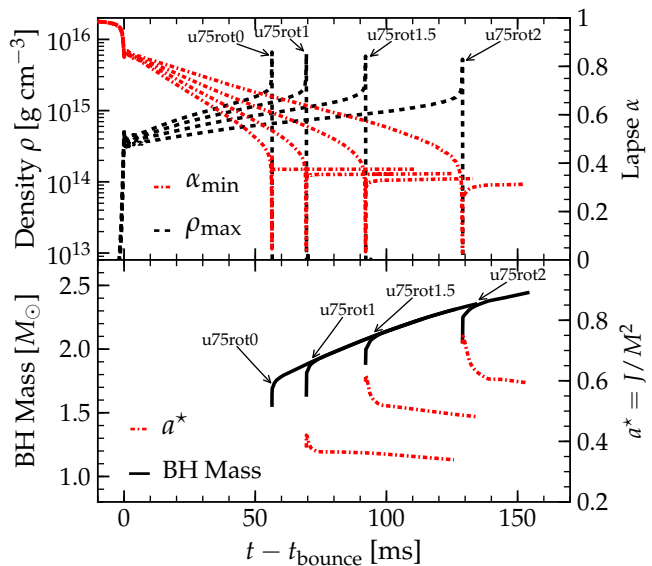


FIG. 2: Top: Maximum density  $\rho_{\max}$  and central ADM lapse function  $\alpha_{\min}$  as a function of postbounce time in all models. After horizon formation, the region interior to it is excluded from min/max finding. Bottom: BH mass and dimensionless spin  $a^*$  as a function of postbounce time. All models follow the same accretion history once a BH forms and settles down. The data shown in this figure are from the LR runs since these were carried out longest after BH formation.

TABLE I: Model summary.  $\Omega_0$  is the initial central angular velocity.  $t_{\text{BH}}$  is the time after bounce to BH formation.  $M_{\text{max}}$  is the mass of the PNS at that time.  $a_i^*$  and  $a_e^*$  are the dimensionless BH spin shortly after BH formation and when the simulation is stopped, respectively.  $E_{\text{GW}}$  is the emitted GW energy and  $f_c$  is the characteristic GW frequency [25] in aLIGO.

Model	$\Omega_0$ [ $\text{rad s}^{-1}$ ]	$t_{\text{BH}}$ [ms]	$M_{\text{max}}$ [ $M_{\odot}$ ]	$a_i^*$	$a_e^*$	$E_{\text{GW}}$ [ $10^{-7} M_{\odot} c^2$ ]	$f_c$ [Hz]
u75rot0	0.0	56.4	1.69	–	–	0.06	591
u75rot1	1.0	68.8	1.82	0.42	0.33	1.1	838
u75rot1.5	1.5	92.1	2.00	0.62	0.48	2.3	848
u75rot2	2.0	129	2.25	0.75	0.59	3.4	807

region, quickly (within milliseconds) succumbs to the ram pressure of the outer core, which is accreting at a rate of initially tens of  $M_{\odot} \text{ s}^{-1}$ . The shock stalls at only  $\lesssim 50$  km and gradually retracts in all models. In the top panel of Fig. 2, we plot the maximum rest mass density  $\rho_{\max}(t)$  that rapidly increases as accreted material settles onto the outer PNS core. The slope of  $\rho_{\max}$  is steepest in the nonrotating model whose PNS becomes unstable earliest. In rotating models, centrifugal effects lead to an oblate and less compact PNS that contracts more slowly and is stable to larger mass (cf. [12, 26] and Table I). The time to BH formation and the maximum PNS mass increase roughly with  $\Omega_0^2$ .

Once dynamical PNS collapse sets in, an apparent

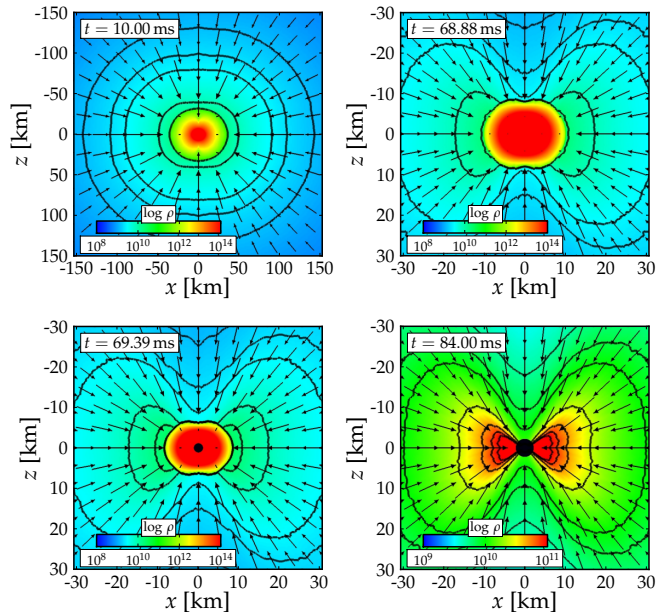


FIG. 3: Snapshots of the meridional density distribution with superposed velocity vectors in model u75rot1 taken at various times. The top left panel (note its special spatial range) shows a snapshot from 10 ms after bounce. The top right and bottom left panels show the point of PNS instability and the time at which the AH first appears, respectively. The bottom right panel, generated with a separate color range, shows the hyperaccreting BH at  $\sim 15$  ms after its formation. All colormaps have density isocontours superposed at densities (from outer to inner) of  $\rho = (0.1, 0.25, 0.5, 0.75, 1.0, 2.5, 5.0) \times 10^{10} \text{ g cm}^{-3}$ .

horizon (AH) appears within  $\sim 1$  ms and quickly engulfs the entire PNS. With the PNS and pressure support removed, postshock material and the shock itself immediately subside into the nascent BH. The bottom panel of Fig. 2 shows the evolution of BH mass and dimensionless spin  $a^*$  in all models. The former jumps up as the AH swallows the PNS and postshock region, then increases at the rate of accretion set by progenitor structure and is largely unaffected by rotation at early times. The dimensionless spin reaches a local maximum when the BH has swallowed the PNS core, then rapidly decreases as surrounding lower- $j$  material plunges into the BH. This is a consequence of the drop of  $j$  at a mass coordinate close to the initial BH mass (cf. Fig. 1). Table I summarizes for all models the values of  $a^*$  at its peak and at the time we stop the LR run.

In Fig. 3, we plot colormaps of the density in the meridional plane of the spinning model u75rot1 taken at various postbounce times. The rotational flattening of the PNS is significant and so is the centrifugal double-lobed structure of the post-BH-formation hyperaccretion flow. The latter is unshocked and far sub-Keplerian with inflow speeds of up to  $0.5c$  near the horizon. The flow will be shocked again only when material with sufficiently

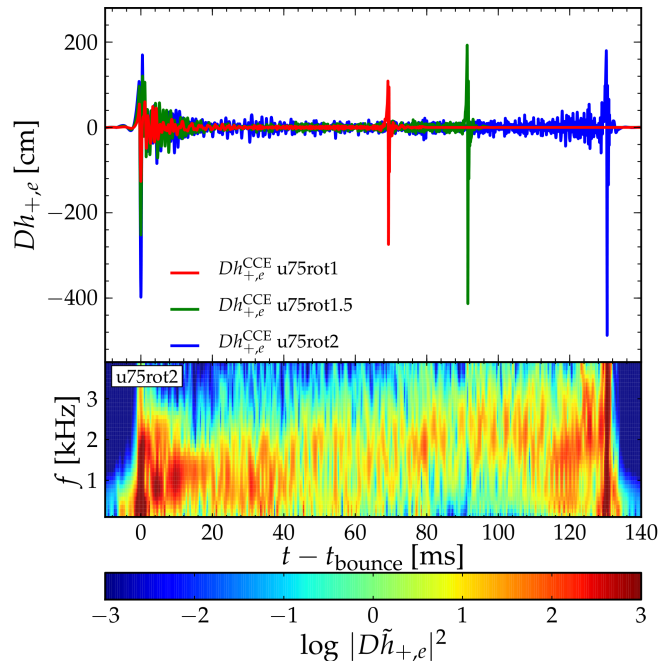


FIG. 4: Top: GW signals  $h_{+,e}$  emitted by the rotating models as seen by an equatorial observer and rescaled by observer distance  $D$ . Bottom: Spectrogram of the GW signal emitted by the most rapidly spinning model u75rot2.

high specific angular momentum to be partly or fully centrifugally supported reaches small radii (cf. [16]). Based on progenitor structure, our choice of rotation law, and the assumption of near free fall, we estimate that this will occur after  $\sim 1.4$  s,  $\sim 2.4$  s,  $\sim 3.9$  s in model u75rot2, u75rot1.5, u75rot1, respectively. At these times, the BHs, in the same order, will have a mass ( $a^*$ ) of  $\sim 8 M_{\odot}$  (0.75),  $\sim 14 M_{\odot}$  (0.73), and  $\sim 23 M_{\odot}$  (0.62).

*GW Signature.*—The top panel of Fig. 4 depicts the GW signals emitted by our rotating models. Due to the assumed octant symmetry, GW emission occurs in the  $l = 2, m = 0$  mode. The nonrotating model leads to a very weak GW signal and is excluded. At bounce, a strong burst of GWs is emitted with the typical signal morphology of rotating core collapse (e.g., [27]) and the peak amplitude is roughly proportional to model spin. Once the bounce burst has ebbed, the signal is dominated by emission from turbulence behind the shock. It is driven first by the negative entropy gradient left by the stalling shock and then by neutrino cooling, whose effect may be overestimated by our simple treatment. Interestingly, the signal strength increases with spin. This is not expected in a rapidly spinning ordinary 2D CCSN, since a positive  $j$  gradient in the extended postshock region stabilizes convection. In our models, the postshock region is considerably smaller and shrinks with postbounce time. The driving entropy gradients are steeper and the change of  $j$  in the postshock region is smaller. Also, in contrast to 2D, our 3D models allow high-mode nonaxisymmetric circulation. We surmise that the combination of these features with increasing spin (feeding greater cir-

ulation) results in a stronger GW signal.

The intermittent period of turbulent, low-amplitude GW emission ends when PNS collapse sets in, leading to a second pronounced spike in the waveform, marking BH formation. The collapse signal evolves into the ring-down emission of the nascent BH that rapidly assumes Kerr shape. The GW emission ceases soon after and the un-shocked axisymmetric accretion flow does not excite, at appreciable amplitude, BH quasi-normal modes that could emit GWs. The strength of the BH formation signal scales with  $\Omega_0$  and its  $dE_{\text{GW}}/df$  peaks at  $\sim 3.9$  kHz,  $\sim 3.4$  kHz,  $\sim 2.9$  kHz, in u75rot1, u75rot1.5, and u75rot2, respectively. The lower panel of Fig. 4 shows the spectrogram of the GW signal in model u75rot2. There is a clear trend towards higher frequencies during the postbounce pre-BH phase, but BH formation itself, while peaking in the kHz range, leads to significant emission also at lower frequencies, which is favorable for detection by advanced laser-interferometer GW observatories (aLIGOs). In Table I, we provide quantitative results on the GW emission in our model set. For an event at 10 kpc, we estimate optimal single-detector aLIGO signal-to-noise ratios (see [17, 25]) of  $\sim 36$  (u75rot1),  $\sim 68$  (u75rot1.5), and  $\sim 94$  (u75rot2), and  $\sim 6$  for the nonrotating model u75rot0. Note that real GW burst searches will not recover all available signal power.

*Discussion.*—We have performed self-consistent 3 + 1 GR simulations of stellar collapse in the context of the collapsar scenario for LGRBs. Albeit approximate in many aspects, our models elucidate characteristic qualitative features in the dynamics and GW signature of these events. The rotating-collapse–bounce–PNS-phase–BH-formation–hyperaccretion sequence and its GW signature are robust aspects of the early collapsar evolution. More realistic physics will undoubtedly affect quantitative results, but the overall qualitative picture is unlikely to change. The characteristic GW signature seen in our models will enable aLIGO to distinguish between a successful and failed CCSN purely on the basis of observed GWs, provided the event is sufficiently nearby.

A more realistic, stiffer EOS will increase the delay between bounce and BH formation and will lead to higher-amplitude, lower-frequency GWs. An improved neutrino treatment may reduce the vigor of turbulence in the PNS phase and decrease the amplitudes of the associated GW signal. Symmetry-free 3D evolution could reveal nonaxisymmetric dynamics that may lead to an enhanced GW signal [27]. Only the inclusion of MHD may lead to a large qualitative change by potentially leading to a strong explosion, leaving behind a magnetar [6, 28, 29]. This study is a first pioneering step and much work lies ahead before a clear and quantitative picture of the CCSN-LGRB connection can be drawn.

This work was supported in part by NSF under grant nos. AST-0855535, OCI-0905046, PIF-

0904015, PHY-0960291, and TG-PHY100033 and by the Sherman Fairchild Foundation. The GW signal data are available for download at <http://www.stellarcollapse.org/gwcatalog>.

---

\* Electronic address: cott@tapir.caltech.edu

- [1] S. E. Woosley and J. S. Bloom, *Ann. Rev. Astron. Astrophys.* **44**, 507 (2006).
- [2] C. L. Fryer and A. Heger, *Astrophys. J.* **623**, 302 (2005).
- [3] C. L. Fryer, S. E. Woosley, and D. H. Hartmann, *Astrophys. J.* **526**, 152 (1999).
- [4] S. E. Woosley and A. Heger, *Astrophys. J.* **637**, 914 (2006).
- [5] S.-C. Yoon, N. Langer, and C. Norman, *Astron. Astrophys.* **460**, 199 (2006).
- [6] N. Bucciantini et al., *Mon. Not. Roy. Astron. Soc.* **396**, 2038 (2009).
- [7] S. E. Woosley, *Astrophys. J.* **405**, 273 (1993).
- [8] A. I. MacFadyen and S. E. Woosley, *Astrophys. J.* **524**, 262 (1999).
- [9] E. Schnetter, B. Krishnan, and F. Beyer, *Phys. Rev. D.* **74**, 024028 (2006).
- [10] T. Fischer et al., *Astron. Astrophys.* **499**, 1 (2009).
- [11] K. Sumiyoshi, S. Yamada, and H. Suzuki, *Astrophys. J.* **688**, 1176 (2008).
- [12] E. O’Connor and C. D. Ott, Submitted to the *Astrophys. J.*, arXiv:1010.5550 [astro-ph] (2010).
- [13] L. Baiotti et al., *Phys. Rev. D* **71**, 024035 (2005).
- [14] Y.-I. Sekiguchi and M. Shibata, *Phys. Rev. D.* **71**, 084013 (2005).
- [15] Y. T. Liu, S. L. Shapiro, and B. C. Stephens, *Phys. Rev. D.* **76**, 084017 (2007).
- [16] Y.-I. Sekiguchi and M. Shibata, *ApJ* submitted; arXiv:1009.5303 [astro-ph] (2010).
- [17] C. Reisswig et al., submitted to *Phys. Rev. D.*, arXiv:1012.0595 [gr-qc] (2010).
- [18] E. Schnetter, S. H. Hawley, and I. Hawke, *Class. Quantum Grav.* **21**, 1465 (2004).
- [19] D. Brown et al., *Phys. Rev. D* **79**, 044023 (2009).
- [20] C. Reisswig et al., *Class. Quant. Grav.* **27**, 075014 (2010).
- [21] H.-T. Janka, T. Zwerger, and R. Mönchmeyer, *Astron. Astrophys.* **268**, 360 (1993).
- [22] P. B. Demorest et al., *Nature* **467**, 1081 (2010).
- [23] J. W. Murphy, C. D. Ott, and A. Burrows, *Astrophys. J.* **707**, 1173 (2009).
- [24] S. E. Woosley, A. Heger, and T. A. Weaver, *Rev. Mod. Phys.* **74**, 1015 (2002), URL <http://www.stellarevolution.org>.
- [25] K. S. Thorne, in *300 Years of Gravitation*, edited by S. W. Hawking and I. W. (Cambridge University Press, Cambridge, UK, 1987).
- [26] T. W. Baumgarte, S. L. Shapiro, and M. Shibata, *Astrophys. J. Lett.* **528**, L29 (2000).
- [27] C. D. Ott, *Class. Quantum Grav.* **26**, 063001 (2009).
- [28] L. Dessart et al., *Astrophys. J. Lett.* **673**, L43 (2008).
- [29] A. Burrows, L. Dessart, E. Livne, C. D. Ott, and J. Murphy, *Astrophys. J.* **664**, 416 (2007).